Spectrochimica Acta Part B: Atomic Spectroscopy 180 (2021) 106203

Contents lists available at ScienceDirect

Spectrochimica Acta Part B: Atomic Spectroscopy

journal homepage: www.elsevier.com/locate/sab

Monte Carlo simulation for the analysis of various solid samples using handheld X-ray fluorescence spectrometer and evaluation of the effect by environmental interferences

Woojin Kim [a,*], Jaeyeong Jang [a], Do Hyun Kim [b]

[a] Korea Institute of Nuclear Nonproliferation and Control, 1534, Yuseong-daero, Yuseong-gu, Daejeon 34054, Republic of Korea
[b] Korea Atomic Energy Research Institute, 111, Deadeok-daero 989 beon-gil, Yuseong-gu, Daejeon, 34057, Republic of Korea

ARTICLE INFO

Keywords:
Nuclear Forensics
Nuclear material
Handheld-XRF
Environmental interferences
Monte Carlo simulation

ABSTRACT

Handheld X-ray fluorescence (HH-XRF) has expanded its utilization areas according to recent technological developments. Most current applications, though, are still concentrated in traditional areas including mineral resource analysis and environmental regulation rather than forensic science for the purpose of investigating a nuclear security event involving nuclear material out of regulatory control. To apply HH-XRF to nuclear material analysis, it is necessary to first obtain calibration data using standard reference materials. Considering the difficulty in obtaining such standard reference materials as well as the high costs involved, one well-known alternative method is to use Monte Carlo simulation code. This study investigated the feasibility of employing Monte Carlo N-Particle transport 6 (MCNP6) simulation to provide calibration data through comparison with experimental measurements of pure solid samples of graphite, copper, SiO_2, and UO_2 using HH-XRF. The results showed that the MCNP6 simulation results were entirely consistent with the measurement spectra, except for environmental interferences stemming from interactions with the mechanical components below 10 keV which varied slightly according to sample type. To quantitatively evaluate the effect of these environmental interferences on the whole spectrum, the coefficient of determination (R^2) was used. In the case of graphite, the effect of the environmental interferences was evaluated to be about 20% on the conformity of the measured and simulated results, while those for copper, SiO_2, and UO_2 were about 1%, 3%, and less than 1%, respectively. These results indicate that samples having elements with higher rates of photoelectric absorption followed by fluorescence compared to scattering tend to decrease the effect of the environmental interferences over the entire spectrum. The origin of the environmental interferences was estimated to be interference with the detector shield and/or X-ray tube collimator, which are particular design features of the device used. Their effect on contributing to the environmental interferences was evaluated by experiment for the detector shield and simulation for the X-ray tube collimator. As the detector shield was found to only contribute to a decrease in overall spectrum intensity, the major contributor to the environmental interferences was determined to be the collimator. It is believed that the results of this study will help to confirm that Monte Carlo simulation can properly provide calibration data for using HH-XRF on nuclear materials for which reference materials are hard to obtain.

1. Introduction

As X-ray tube and detector technologies have become more sophisticated, handheld X-ray fluorescence (HH-XRF) applications have expanded [1–5]. For instance, HH-XRF has become a type of forensic science equipment, with several applications including gunshot residue analysis, glass fragment analysis, and the matching of samples associated with suspects or crime scenes [6]. In the field of nuclear security, while XRF techniques have been proposed for use in nuclear forensics in cases encountered out of regulatory control [7], however, related applications have focused on desktop types of analytic tools in the laboratories and have not considered handheld types of equipment for usage in the field. Absolutely, desktop equipment in laboratory settings provides more accurate and therefore confident performance than handheld types; however, such large equipment involves high costs and is generally hard to use after moving into the crime scene. Furthermore,

* Corresponding author.
E-mail address: kimwj@kinac.re.kr (W. Kim).

https://doi.org/10.1016/j.sab.2021.106203
Received 14 August 2020; Received in revised form 9 April 2021; Accepted 12 April 2021
Available online 16 April 2021

Table 1
Specifications of the experimental samples.

Sample	Type	Density	Certifying Agency	Serial Number
Graphite	Solid/Cylinder	2.26 g/cm^3	FLUXANA	FI001953
Copper	Solid/Cylinder	8.96 g/cm^3	FLUXANA	FM0011942
SiO_2	Solid/Sample cup (powder)	2.65 g/cm^3	Sigma-Aldrich	MB060-50G
UO_2	Solid/Cylinder	10.5 g/cm^3	KEPCO Nuclear Fuel	8F2H364

samples containing nuclear material or radioactively contaminated material are often not able to be safely handled in laboratories or loaded into equipment due to issues with cross-contamination and safety regulations. It is therefore important to conduct an in-situ preliminary analysis to minimize the safety risks of first responders and establish appropriate analytical plans prior to the collection, sampling, and transport of such materials to forensic laboratories. In this light, HH-XRF equipment can be an effective analytical tool that can provide an elemental characteristic of various types of samples can be detected practically in the field.

To date though, HH-XRF has rarely been used for nuclear material analysis, particularly when the nuclear material is meant to include uranium, plutonium, or thorium as major constituents. In order to apply HH-XRF to nuclear material for elemental analysis, additional optimization work is requisite because there currently is insufficient calibration data for nuclear material samples to determine and quantify elemental composition. Some researchers have produced experimental data directly through measurements of standard reference materials (SRMs) or synthetic samples made by themselves [8–10]. Most studies involved liquid samples dissolved by nitric acid or the content analysis of uranium and plutonium mixtures. For any such studies, it is not easy to obtain the relevant SRMs and then conduct the desired experiments, since all nuclear material is rigorously controlled by international norms and national regulations.

Considering these difficulties, Monte Carlo simulation has long been an alternative method to conducting experiments with sensitive nuclear materials. In terms of X-rays, most simulations focus on the estimation of X-ray beam profiles produced from X-ray tubes for managing the radiation exposure of patients and workers; such beam profile estimation has been known to achieve high accuracy from X-ray sources [11–13]. However, additional design parameters for HH-XRF such as geometry and material compositions, need to be considered in detail to more precisely simulate the energy spectrum that results from the detector. Such data are not opened to the public nor to equipment users, though, because they include the manufacturers' know-how.

The purpose of this study is to simulate the X-ray energy spectra of a range of samples using openly available data and then verify the feasibility of the simulation by comparing the results to experimental measurements. To do so, spectra of graphite, copper, SiO_2, and UO_2 solid samples were experimentally collected using HH-XRF and compared with Monte Carlo simulation results. During the investigation, unexpected fluorescence peaks stemming from interactions with the instrumentation, which is called environmental interferences [14], were identified in all measurement spectra but not in simulation; the effects of these peaks on the measurement performance for each sample were evaluated using the coefficient of determination (R^2). From this simulation study, it is expected that the energy spectra of nuclear material samples, with which experimental measurements are not easily conducted, can be obtained.

2. Materials and methods

2.1. Samples

The samples used in this study were graphite, copper, SiO_2, and UO_2, as shown in Table 1. Graphite and copper were selected as representative pure single elements, obtained as reference materials from FLUXANA. In particular, graphite was selected as a blank sample presenting a background spectrum when other elemental samples are measured. It is predicted to give a reasonable approximation of the original beam profile produced by the X-ray tube due to the X-ray scattering properties of materials with low atomic numbers and the relatively low energy of X-ray fluorescence. Copper belongs to the transitional metals having very high fluorescence rates, so its use was expected to reveal related phenomena by interactions in the detector such as sum peaks. SiO_2 represents one of the major matrix elements in geological samples. The material of interest, UO_2, is the major chemical form conventionally used in the commercial nuclear fuel cycle, constituting the fuel rods in many nuclear power plants.

2.2. Instruments

A Bruker S1-Titan 600 handheld XRF analyzer (Bruker, Billerica, MA, USA) was used for the experimental measurements. It consists of a fast silicon drift detector (SDD), an ultralene beryllium (Be) window, and an end window transmission type X-ray tube with the following specifications: Maximum accelerating voltage 50 kV, Maximum power 2 W, and Rhodium (Rh) target with 0.65 μm of thickness and 1.85 g/cm^3 of density. In this study, the spectrometer mode without any calibration was used. A desktop kit provided by the manufacturer was also used to achieve controlled measurement geometry.

2.3. Experimental setup

A number of parameters can influence the beam profile irradiated into samples from the X-ray tube as well as the result energy spectrum measured by the SDD. These parameters include accelerating electron voltage, current, measured time, applied filters, and mechanical components. The voltage and filters directly influence the incident X-ray beam in both energy distribution and intensity, while current and measuring time are proportional to the intensity at each energy interval.

This study selected the no filter option because it is more convenient to minimize any interference factors for ease of comparison with the Monte Carlo simulation results. Accelerating electron voltage was set at 50 kV, while current and operating time were fixed at 35 μA and 30 s in the real-time setting except for the UO_2 sample, for which 60 s was set. The HH-XRF device used in this study does not provide a function to control live-time; rather, the real-time setting is applied as an experimental setup parameter and then normalized for comparison with simulations. Here, real time means the actual time which has elapsed between starting and stopping a measurement, while live time represents an estimate of the total effective time that the digital pulse processor could have been acquiring valid counts. All experimental parameters were maintained in the same conditions.

2.4. Monte Carlo simulation

By analyzing the energy spectrum obtained from simulations of the experimental measurements, the feasibility of applying simulation to the measurement of nuclear material was evaluated. HH-XRF measurements were simulated using Monte Carlo N-Particle Transport Code System version 6.2.0 (MCNP6, Los Alamos National Lab, NM, USA). The cross-section library used to compute the transport of electrons and photons was the Electron Photon Relaxation data 14 (EPRDATA14) library.

2.4.1. Profiling of the X-ray source beam

Fig. 1 presents the variation of the X-ray beam geometric size generated by the HH-XRF device according to the increasing distance from the beam port [15]. Generally, manufacturers provide this kind of radiation profile to let users know about the radiological conditions during instrument operation. This information is obtained from radiation measurements using a radiation survey instrument in accordance with the IEC62495 which have been used for their licensing.

Considering the X-ray tube specifications and parameters, X-ray beam generation was simulated using MCNP6 code. The thickness and density of the Rh target were set to 0.65 μm and 12.41 g/cm^3, respectively, and the thickness and density of the beryllium (Be) window were 125 μm and 1.85 g/cm^3, respectively. The accelerating voltage of electrons was set to 50 kV, same as in the experiment. The electron beam was assumed to be incident vertically to the center of the Rh target in a vacuum.

To calculate the energy distribution of the primary X-ray beam emitted from the Rh target, which is often called the primary X-ray beam source profile or open beam profile, the number of X-rays passing through the surface corresponding to the incidence angle range of the X-ray beam was obtained using F1 tally in MCNP6. The tally card is a function to specify what type of information the user wants to gain from the Monte Carlo calculation, and the F1 tally is a card that calculated the current integrated over a surface. The incidence angle of the X-ray beam was set to 20 degrees as shown in Fig. 1, by referring to the manual of HH-XRF. The relative intensity by X-ray energy on the surface was calculated. Based on these calculation results, Fig. 2 shows the primary X-ray beam source profile calculated for both vacuum and air media. The former represents the X-rays immediately after emission from the Rh target, while the latter represents reflection by air of the X-rays between the HH-XRF and the contact surface of the sample.

2.4.2. Material and geometry setup

The simulation was also performed by MCNP6 using an F8 Tally (Pulse Height Tally) card which derives the output of the energy distribution of pulses created by radiation in a detector. MCNP6 was used to simulate the energy spectrum generated by the detector. It was derived from the specifications provided by the manufacturer [16,17] such as the incidence angle of the X-ray, the placement of the detector, and the distance between the major components in the HH-XRF device. The detector was assumed to consist of pure silicon in a cylindrical shape of size 0.51 cm × 0.05 cm (diameter × length), as referenced from the specifications of the SDD in the HH-XRF equipment. The energy spectra measured via HH-XRF for all samples were obtained through the simulation using the primary X-ray beam source profile from Section 2.4.1.

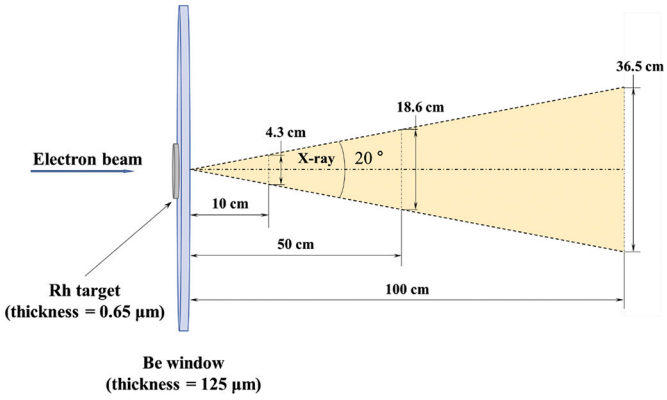

Fig. 1. Schematic of the emission angle and diameter of the X-ray beam at various distances from the beam port [15].

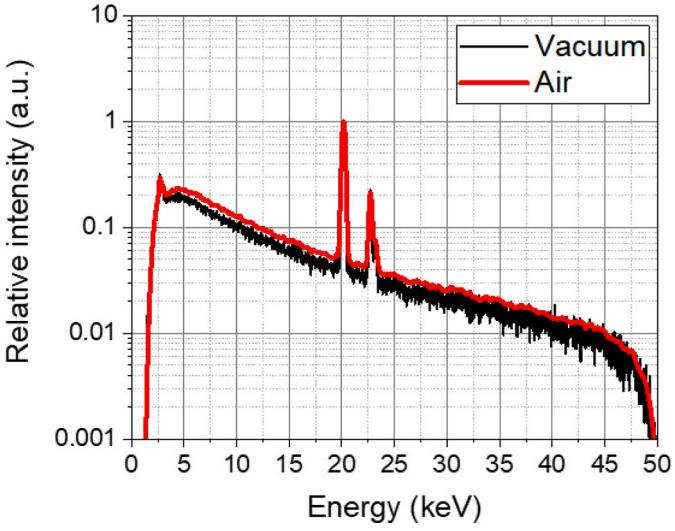

Fig. 2. Primary X-ray beam source profile through MCNP6 simulation for vacuum and air media. The accelerating voltage is 50 kV.

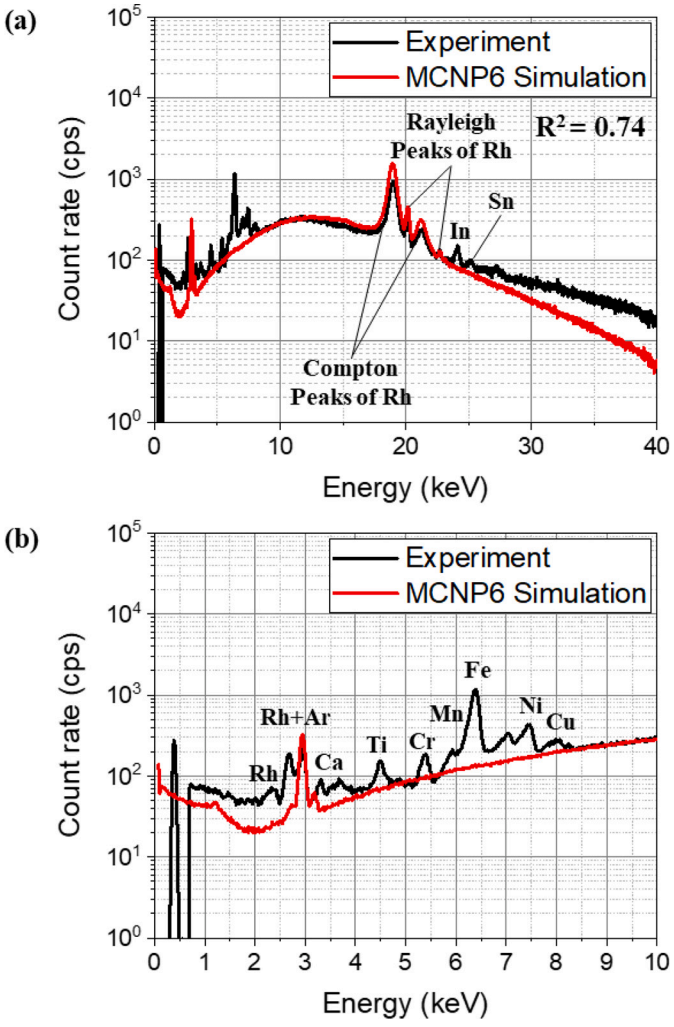

Fig. 3. Measured energy and MCNP6 simulation spectra for the graphite sample at energy ranges (a) 0–40 keV and (b) 0–10 keV. The accelerating voltage was 50 kV and the filter option was not selected.

3. Results

3.1. Energy spectra of experiment and MCNP6 simulation

3.1.1. Graphite

Fig. 3 shows a comparison between the experimental and simulated spectra of the graphite sample. The main difference is the existence of environmental interferences stemming from interactions with the instrumentation, which are existed in the experiment but absent in simulation. This is because, in the MCNP6 simulation, only the results of scattering and fluorescence by the primary X-ray incident on the graphite sample were calculated. The conformity of the spectra was evaluated through the coefficient of determination (R^2). For the entire energy range (0–40 keV), the R^2 was 0.744. For the energy range excluding up to 10 keV, where the environmental interferences were mainly generated, the R^2 was 0.946. The result shows that the environmental interferences had about a 20.2% effect on the conformity of the energy spectra in the case of the graphite sample.

3.1.2. Copper

Fig. 4 shows a comparison between the experimental and simulated spectra of the copper sample. The sum peaks indicating that the peaks occurred experimentally due to limitations in detector resolution, present in the experimental results but did not appear in the MCNP6 simulation. For the entire energy range, the R^2 was 0.977, showing a high similarity of the spectra. In the range from 0 keV to 10 keV, without the sum peaks, the R^2 was 0.985. This result indicates that the environmental interferences under 10 keV and the sum peaks had relatively little effect on conformity, and accordingly, the MCNP6 simulation shows high accuracy for the copper sample.

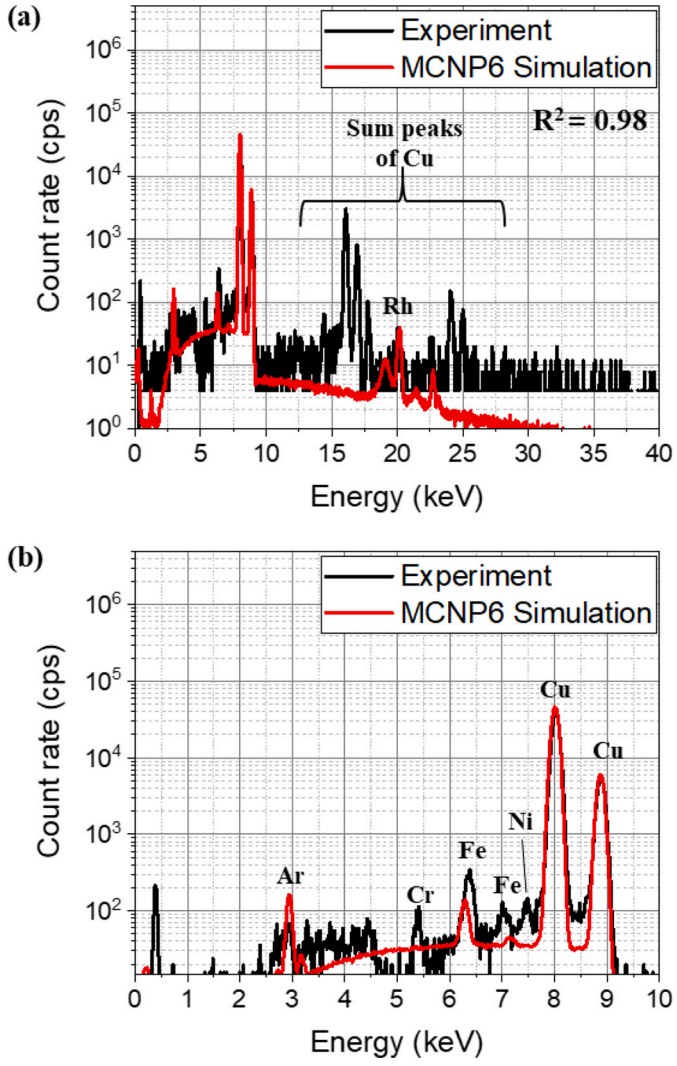

Fig. 4. Measured energy and MCNP6 simulation spectra for the copper sample at energy ranges (a) 0–40 keV and (b) 5–20 keV. The accelerating voltage was 50 kV and the filter option was not selected.

3.1.3. SiO_2

Fig. 5 shows a comparison of the simulated and experimental spectra of the SiO_2 sample. The main difference between the results was caused by the environmental interferences, like in the previous cases. Since normalization was performed based on the peak of silicon Kα1 fluorescence at 1.74 keV, a difference occurred at the Compton peak of the Rh K line. For the entire energy range, the R^2 was 0.900. Excluding the range of 3.1 keV to 9 keV, where the environmental interferences were mainly generated, analysis of conformity gave an R^2 of 0.930, meaning that the effect of the environmental interferences on the conformity of the SiO_2 spectra is about 3%.

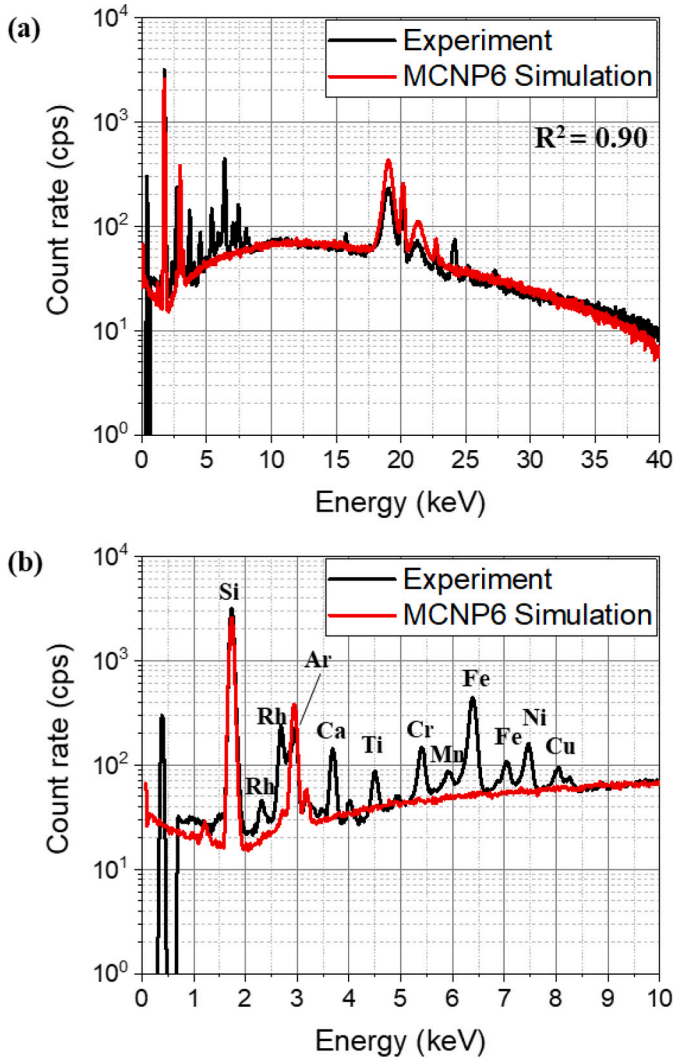

Fig. 5. Measured energy and MCNP6 simulation spectra for the SiO_2 sample at energy ranges (a) 0–40 keV and (b) 0–10 keV. The accelerating voltage was 50 kV and the filter option was not selected.

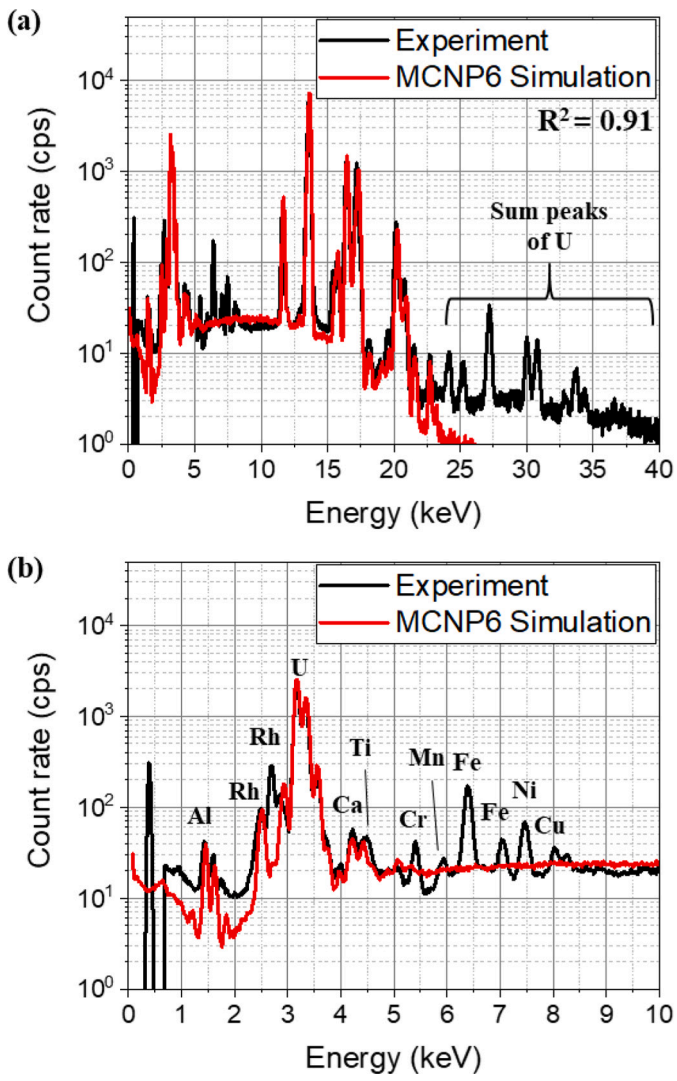

Fig. 6. Measured energy and MCNP6 simulation spectra for the UO_2 sample at energy ranges (a) 0–40 keV, (b) 0–10 keV. The accelerating voltage was 50 kV and the filter option was not selected.

3.1.4. UO_2

Fig. 6 shows a comparison of the simulated and experimental spectra of the UO_2 sample. Similar to the copper sample, the difference due to the environmental interferences was not large. The peaks of the uranium L and M lines showed high agreement between the experiment and MCNP6 simulation. Over the entire energy range, the R^2 was 0.906. Analyzing the conformity excluding the range 3.5–9 keV where the environmental interferences were mainly generated, the R^2 was 0.906. This means that the environmental interferences have little effect on spectral conformity in the case of the UO_2 sample.

All spectra of each sample's measurements are shown in Fig. S1-S4 (Appendix). Additional efforts to find out their origin are discussed in Section 4.

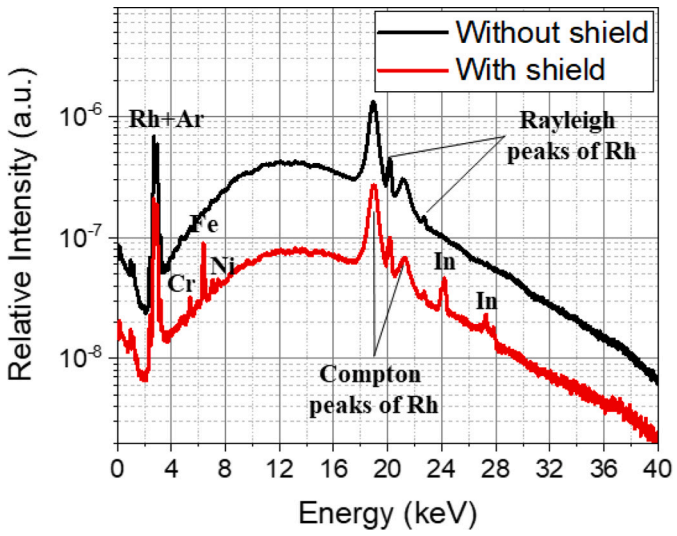

Fig. 8. Comparison of energy spectra with and without the detector shield.

4. Discussion

4.1. Origins of the environmental interferences

In all experimental spectra, the unexpected fluorescence peaks by environmental interferences generally depend on the sample type. In particular, these environmental interferences have a large effect on conformity in the graphite sample. So, the graphite sample was selected at first, then other samples are included for further simulation in this discussion chapter. As shown in section 3.1.1, the energy spectrum measured by graphite sample is best to let us know what is difference between the experiment and simulation because of its simple interaction with primary X-ray.

It is derived below that they are produced by interference with the

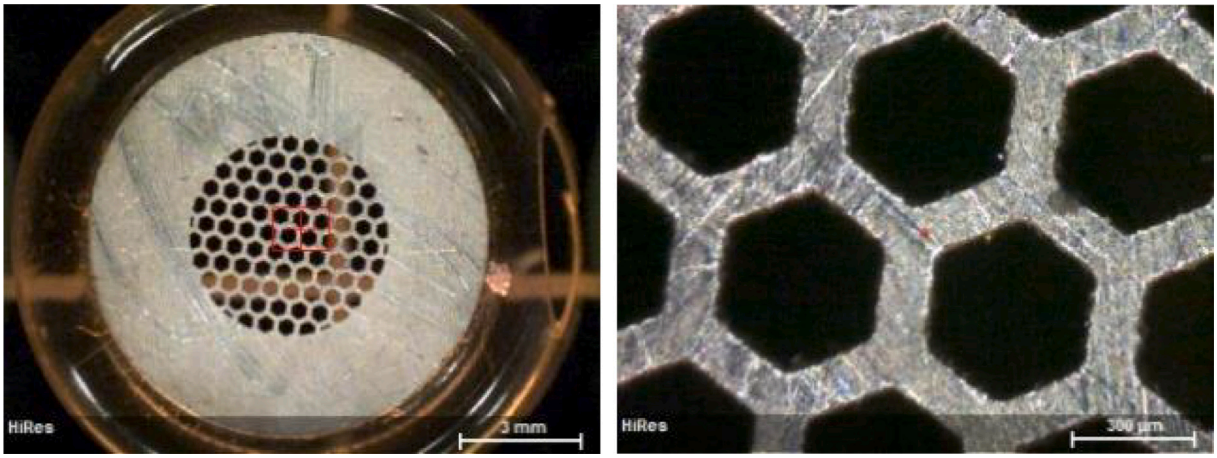

Fig. 7. Images of the detector shield. Scale bars are 3 mm (left) and 300 µm (right).

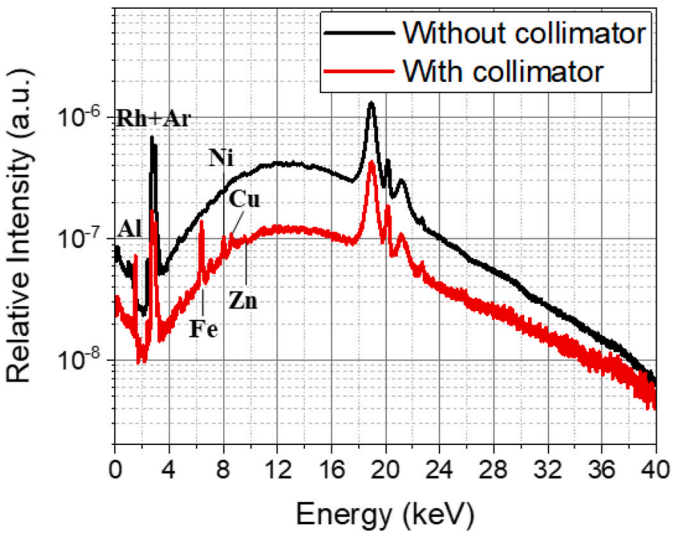

Fig. 9. Comparison of energy spectra with and without the collimator.

instrumentation; considering the design features of the HH-XRF equipment, two possible origins are investigated as the major origins of the environmental interferences.

The first possible origin was estimated to be interference from the detector shield, which protects the detector window from being punctured by sharp objects. To confirm this estimation, the detector shield was extracted from the detector, as shown in Fig. 7, for elemental composition analysis by a Bruker M4 Tornado Micro-XRF analyzer (Bruker, Billerica, MA, USA). The elemental composition by weight percent was calculated as Fe (51.19 wt%), Cr (9.65 wt%), Ni (6.84 wt%), and In (25.94 wt%).

Using the MCNP6 code, the detector shield was applied as shown in Fig. 10(a) to simulate the measurement of the graphite sample. As previously calculated, an energy spectrum was obtained by specifying SDD as F8 tally as shown in Fig. 8. As a result of the simulation applying the detector shield, it is confirmed that the shield affects a decrease in intensity across the entire spectrum. In addition, fluorescence peaks by Fe, Cr, Ni, and In are obviously observed. These peaks are due to the fluorescent X-ray generated from the detector shield in that they were not present in the case without the shield. Especially, it is determined that Fe and In mainly affect due to their high content. Therefore, it could be confirmed that some of the environmental interferences are caused by the detector shield.

The second possible origin was estimated to be interference from the X-ray tube collimator that sharpens the beam and makes it closer to the sample in the employed device than in traditional designs. To confirm this estimation, an additional MCNP6 simulation was performed to identify the extent that the collimator may produce environmental interferences. The element composition of the collimator was analyzed using the M4 Tornado Micro-XRF analyzer for the simulation. The element composition of the inner collimator by weight percent was calculated as Al (97.12 wt%), Fe (2.16 wt%), and traces of other elements such as Ca, Cu, Ni. The composition of the outer collimator was calculated as Cu (60.82 wt%), Zn (36.4 wt%), Pb (2.59 wt%), and Fe (0.19 wt%). The element composition data of the collimator was applied and the simulation was performed. The energy spectrum calculated by specifying SDD as F8 tally as shown in Fig. 9 presents that there are fluorescent X-ray peaks by Fe, Cu, Ni, and Zn below 10 keV. Especially, it is determined Al and Fe mainly affected due to their high content. The result of the simulation shows that the environmental interferences can arise from interference with the collimator in response to the primary X-ray source beam.

Additional simulation was applied using both tentative two origins as shown in Fig. 10 in order to confirm the effcts of both the detector shield and collimator at the same time. Fig. 11 shows the energy spectra of both experiment and simulation, normalized assuming they have the same total count rate. Compared to the simulated spectrum shown in Fig. 3, it could be seen that it is quite similar to the energy spectrum obtained by the experiment. Environmental interferences, which mainly occur in the 0–10 keV energy range, were also simulated fairly well, and the continuous spectrum in the energy region of 25 keV or more showed good agreement. As a result, the coefficient of relation (R^2) is 0.930, which is 19% higher than the previous R^2 of 0.744.

Fig. 12 shows the energy spectra of both experiment and simulation, normalized assuming they have the same total count rate. As in the case of the graphite sample, environmental interferences were well simulated. For the entire energy range, R^2 was 0.974, 0.969, and 0.904.

In the case of graphite and SiO_2 samples, the difference of R^2 between the improved simulation and existing simulation was noticeable at 15% and 4%. On the other hand, in the case of copper and UO_2 sample, since the intensity of the secondary X-ray generated by the sample was much higher than that of X-ray from environmental interferences, there was little difference of R^2 between the improved simulation and existing simulation. In other words, the influence of environmental interferences had less effect.

4.2. *Variation of environmental interferences by sample type*

To observe the variation in the environmental interferences by the type of sample, comparisons were made to distinguish the excitation spectra between elements in the samples and elements from instrument contribution, as shown in Fig. 13. All samples contain common spectra from Cr, Mn, Fe, Ni, and Cu. By normalizing the spectra to the intensity of the graphite spectrum at 6.4 keV, the heights of the Fe Kα lines, the

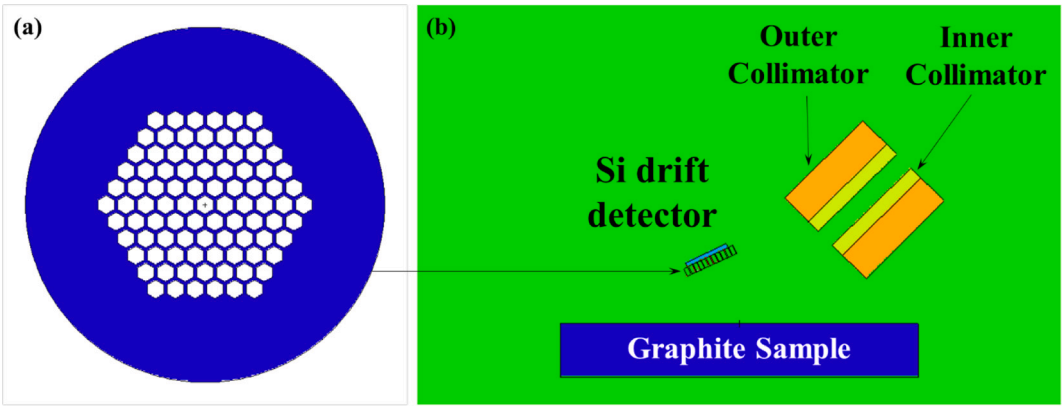

Fig. 10. Cross-sectional view of the MCNP6 geometry model of (a) the detector shield and (b) the entire simulation.

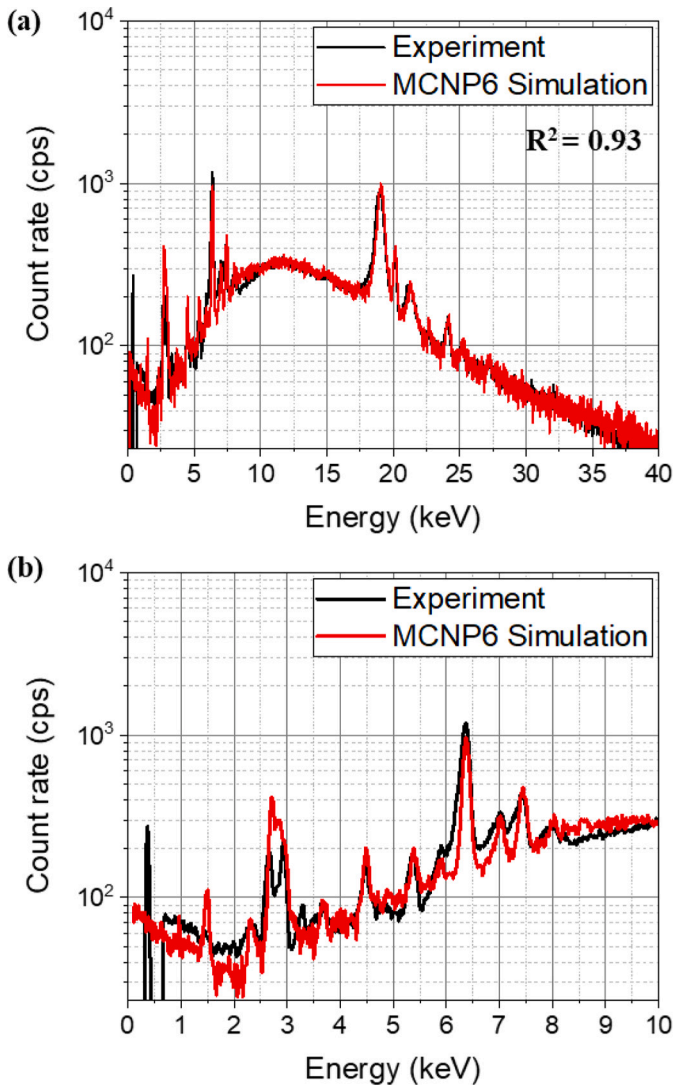

Fig. 11. Comparison of measured and simulated spectra of graphite to check the effect of collimator and detector shield at energy ranges (a) 0–40 keV, (b) 0–10 keV.

highest can be compared more easily. From the normalized spectra, it is observed that the environmental interferences do not significantly deviate by sample, except for the UO_2 spectrum which suggests contributions from not only elements in the sample but also the instrument itself.

Section 3.1 above presented the results of conformity evaluations of the measured and simulated energy spectra. The former represents the real case with environmental interferences while the latter is the ideal case without those. In conclusion, it is found their effects to range from 1 to 3% in three samples but up to 18% in the case of graphite. This is because that graphite has rare fluorescence peaks due to low energy and relatively strong scattering peaks from a high yield of the primary X-rays, while the other three samples have strong fluorescence peaks and relatively fewer scattering peaks. This means that their effect depends on the fluorescence peaks of the sample elements having significantly different intensities, as shown in Fig. 14. In addition, for samples containing elements having high fluorescence peaks such as copper and UO_2, the effect of environmental interference is not significant. Thus, high consistency between the measured spectrum and the Monte Carlo simulation is achieved for these samples.

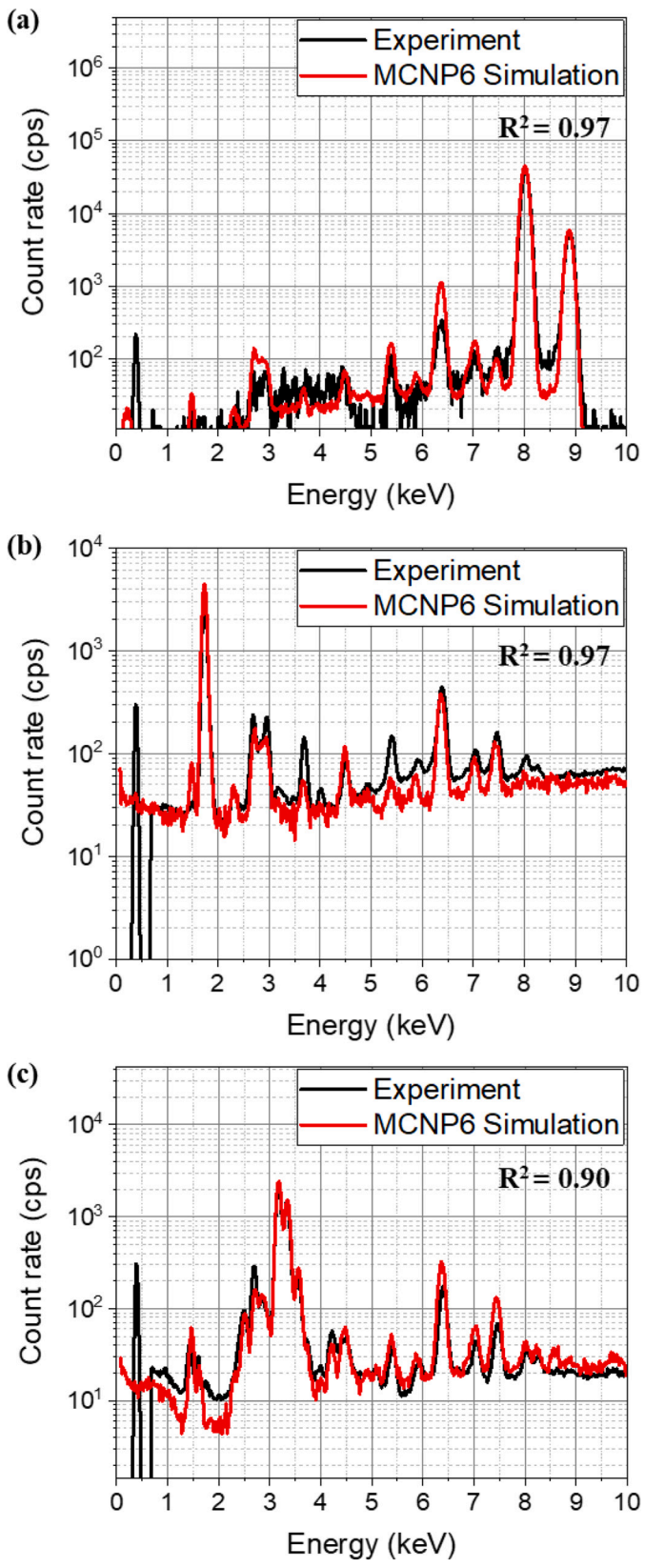

Fig. 12. Comparison of measured and simulated spectra to check the effect of the collimator and detector shield in energy ranges 0–10 keV (a) at the copper sample, (b) SiO_2 sample, and (c) UO_2 sample.

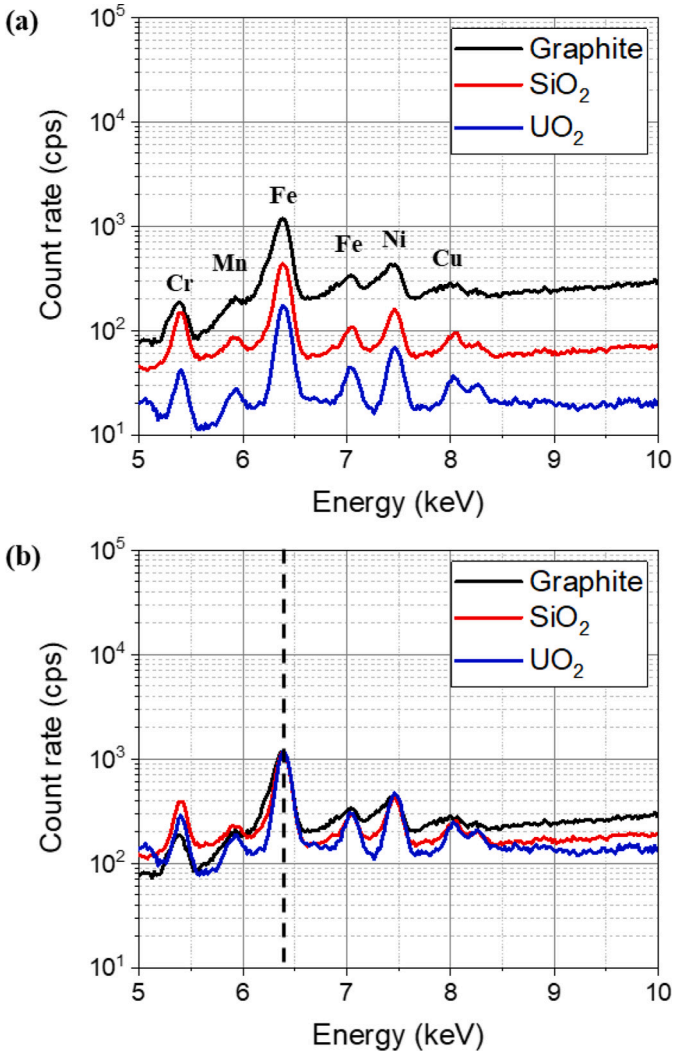

Fig. 13. Excitation spectra from the graphite, SiO_2, and UO_2 samples (a) in the 5–10 keV range, and (b) normalized at about 6.4 keV.

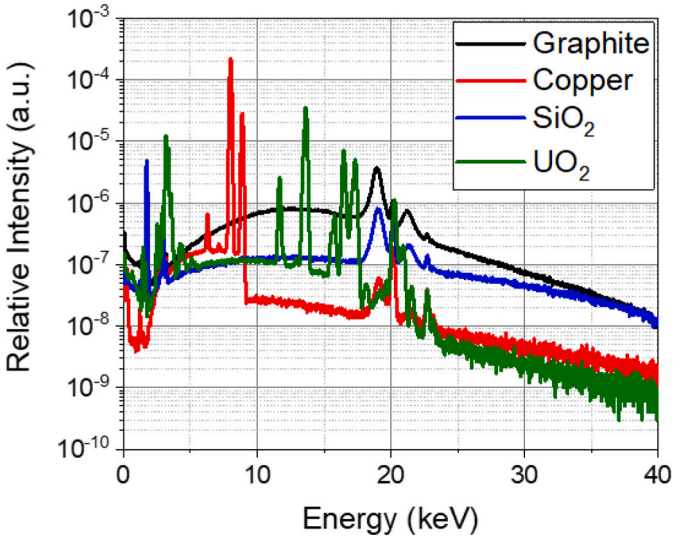

Fig. 14. Excitation spectra to distinguish the elements in the samples.

5. Conclusion

This study investigated the feasibility of applying Monte Carlo simulation to obtain the energy spectra of nuclear samples for use as calibration data by comparing simulation results to experimental measurements using HH-XRF for various pure solid samples.

A Conformity comparison between the normalized energy spectra from simulations and measurements was conducted. The effect of the observed environmental interference on the whole spectrum was evaluated using the coefficient of determination (R^2). It was found that Monte Carlo simulation excluding the low energy range until 10 keV yielded 95% conformity in the graphite case and 99, 93, and 91% conformity for the copper, SiO_2, and UO_2 samples, respectively. The effect of environmental interferences was evaluated to be about 20% in the graphite sample while correspondingly about 1, 3, and less than 1% in the copper, SiO_2, and UO_2 samples. This result indicates that samples having elements with higher rates of photoelectric absorption followed by fluorescence tend to decrease the effect of the environmental interferences over the entire spectrum. Through this investigation, it was determined that the assumptions and design parameters employed in the MCNP6 simulation are feasible to provide energy spectra for use with HH-XRF.

This study applied some assumptions for the Monte Carlo simulation due to a lack of detailed design parameters of the HH-XRF device. These assumptions can also contribute to the incompleteness of simulation results. For more precise prediction by simulation, additional simulations to identify the possible origins of environmental interferences were conducted with more instrument details including the collimator and detector shield with adding in our MCNP6 input geometry. The major differences between simulation and measurement spectra were identified to derive from the environmental interferences below 10 keV. It was estimated that these originated from the detector shield and the X-ray tube collimator, which are particular design features that were not simulated in MCNP6. As a result of the simulation for the detector shield, it could be confirmed that some of the environmental interferences are caused by the detector shield. In the case of the X-ray tube collimator, it was observed that it can also arise from interference with the collimator in response to the primary X-ray source beam. Based on this additional discussion work, it will help for the MCNP simulation to have more accuracy.

The MCNP6 simulations here were conducted using limited data such as user manuals and open information. Nonetheless, they were successful in simulating the primary beam source profile after interaction with Rh targets and electrons, as well as the detector response after interaction with samples except for the environmental interferences stemming from interactions with the instrumentation. However, it is well-known that the primary X-ray beam profile is sensitive and variable as a small design parameter of X-ray tubes [18–20]. Especially, the focal spot size and the distribution of incident electrons to the target may affect the primary beam profile. In addition, the distances among the Rh target, sample, and detector can affect the resulting energy spectrum via detector response. Therefore, it is recommended that further efforts to estimate a more precise source beam profile can contribute to having more accuracy with the Monte Carlo simulation results.

Declaration of Competing Interest

The authors declare that they have no known competing financial interests or personal relationships that could have appeared to influence the work reported in this paper.

Acknowledgements

This work was supported by the Nuclear Safety Research Program through the Korea Foundation of Nuclear Safety (KOFONS) using the financial resource granted by the Nuclear Safety and Security Commission (NSSC) of the Republic of Korea (Grant No. 1804026).

Appendix A. Supplementary data

Supplementary data to this article can be found online at https://doi.org/10.1016/j.sab.2021.106203.

References

[1] M.C. Corbeil, J. Philip, Potts and Margaret west (Eds.): portable X-ray fluorescence spectrometry. Capa for in situ analysis, Anal. Bioanal. Chem. 393 (2009) 1385–1386, https://doi.org/10.1007/s00216-008-2587-6.

[2] Eva Marguí, René Van Grieken, State-of-the-art of X-ray fluorescence instrumentation for chemical analysis, Petro Industry News (2013) 16–18. June/July.

[3] Analytical Methods Committee AMCTB No. 89 (1), hand-held X-ray fluorescence spectrometry, anal, Methods 11 (2019) 2498–2501, https://doi.org/10.1039/C9AY90060H.

[4] International Atomic Energy Agency, In Situ Applications of X Ray Fluorescence Techniques, IAEA-TECDOC-1456, IAEA, Vienna, 2005.

[5] Kelsey E. Young, Cynthia A. Evans, Kip V. Hodges, Jacob E. Bleacher, Trevor G. Graff, A review of the handheld X-ray fluorescence spectrometer as a tool for field geologic investigations on earth and in planetary surface exploration, Appl. Geochem. 72 (2016) 77–87. ISSN 0883-2927, https://doi.org/10.1016/j.apgeochem.2016.07.003.

[6] Criminal Forensics, Bruker, website, https://www.bruker.com/ko/applications/detection-and-environmental/forensics/criminal-forensics.html. (Accessed 9 April 2021).

[7] INTERNATIONAL ATOMIC ENERGY AGENCY, Nuclear Forensics in Support of Investigations, IAEA Nuclear Security Series No. 2-G (Rev. 1), IAEA, Vienna, 2015.

[8] D. Gallhofer, B.G. Lottermoser, The influence of spectral interferences on critical element determination with portable X-ray fluorescence (pXRF), Minerals 8 (2018) 320, https://doi.org/10.3390/min8080320.

[9] J.P. Mondia, F. Goh, P.A. Bryngelson, J.M. MacPhee, A.S. Ali, A. Weiskopfa, M. Lanana, Using X-ray fluorescence to measure inorganics in biopharmaceutical raw materials, Anal. Methods 7 (2015) 3545–3550, https://doi.org/10.1039/C4AY02936D.

[10] Morita Kazuo, Ogawa Yukiharu, Chi N. Thai, Fumihiko Tanaka, Etsuji Ishiguro, Spectral analysis of reflected soft x-ray for detecting foreign materials in foods, Food Sci. Technol. Res. 9 (3) (2003) 231–236. Released March 03, 2007, Online ISSN 1881–3984, Print ISSN 1344-6606, https://doi.org/10.3136/fstr.9.231.

[11] P. Martinelli, J.L. Boutaine, G. Gousseau, J.C. Tanguy, C. Tellechea, Determination of uranium and/or plutonium using X-ray fluorescence analysis excited by 192Ir sealed sources, Nucl. Instruments Meth. Phys. Res. Sec. Accel. Spect. Detect. Assoc. Equip. 242 (3) (1986) 569–573. ISSN 0168-9002, https://doi.org/10.1016/0168-9002(86)90468-7.

[12] J. Py, J.-E. Groetz, J.-C. Hubinois, D. Cardona, Determination of Plutonium in Nitric Acid Solutions Using Energy Dispersive L X-Ray Fluorescence with a Low Power X-Ray Generator. Nuclear Instruments and Methods in Physics Research Section A, Accelerators, Spectrometers, Detectors and Associated Equipment, Apr 2015, pp. 131–137. https://doi:101016/jnima201501073.

[13] A. Pandey, F.A. Khan, A. Kelkar, et al., Determination of trace amounts of uranium in plutonium oxide by wavelength dispersive X-ray fluorescence spectrometry, J. Radioanal. Nucl. Chem. 324 (2020) 731–736, https://doi.org/10.1007/s10967-020-07116-6.

[14] R. Redus, Amptek Inc, Amptek Application Note XRF-1: XRF Spectra and Spectra Analysis Software. https://www.amptek.com/-/media/ametekamptek/documents/resources/application-notes/xrf_2.pdf?dmc=1&la=en&revision=6c68e243-0759-4a6a-abe7-88e489aa2f63. (Accessed 9 April 2021).

[15] Bruker Corporation, S1 Titan Overview. https://www.bruker.com/content/bruker/int/en/products-and-solutions/elemental-analyzers/handheld-xrf-spectrometers/S1-TITAN.html. (Accessed 9 April 2021).

[16] Bruker Corporation, Technical note #1303 Sharp Beam. https://www.technologynetworks.com/analysis/product-news/bruker-introduces-2nd-generation-of-s1-titan-handheld-xrf-analyzer-216583. (Accessed 9 April 2021).

[17] Robert F. Shannon, Jr., Compact collimating device, US patent 8,223,925 B2, filled April 15, 2010, and issued July 17, 2012, https://patents.google.com/patent/US8223925B2/en (accessed 09 April 2021).

[18] M.R. Ay, S. Sarkar, M. Shahriari, D. Sardari, H. Zaidi, Assessment of different computational models for generation of x-ray spectra in diagnostic radiology and mammography, Med. Phys. 32 (6) (2005 Jun) 1660–1675, https://doi.org/10.1118/1.1906126. 16013725.

[19] M. Yücel, E. Emirhan, A. Bayrak, C.S. Ozben, E. Barlas Yücel, Comparison of simulated and measured spectra from an X-ray tube for the energies between 20 and 35keV, Nucl. Instruments Meth. Phys. Res. Sec. Accel. Spect. Detect. Assoc. Equip. 799 (2015) 50–53. ISSN 0168-9002, https://doi.org/10.1016/j.nima.2015.07.055.

[20] Mohammad M. Nasseri, Determination of tungsten target parameters for transmission X-ray tube: a simulation study using Geant4, Nucl. Eng. Technol. 48 (3) (2016) 795–798.